Aqueous co-precipitation of Pd-doped cerium oxide nanoparticles: chemistry, structure, and particle growth

Hongying Liang, Joan M. Raitano, Guanghui He, Austin J. Akey, Irving P. Herman, Lihua Zhang & Siu-Wai Chan

Journal of Materials Science
Full Set - Includes `Journal of Materials Science Letters'

ISSN 0022-2461
Volume 47
Number 1

J Mater Sci (2012) 47:299-307
DOI 10.1007/s10853-011-5798-8

Springer

J Mater Sci (2012) 47:299–307
DOI 10.1007/s10853-011-5798-8

Aqueous co-precipitation of Pd-doped cerium oxide nanoparticles: chemistry, structure, and particle growth

Hongying Liang · Joan M. Raitano · Guanghui He · Austin J. Akey · Irving P. Herman · Lihua Zhang · Siu-Wai Chan

Received: 16 March 2011 / Accepted: 15 July 2011 / Published online: 2 August 2011

Abstract Nanoparticles of palladium-doped cerium oxide (Pd–CeO_2) have been prepared by aqueous co-precipitation resulting in a single phase cubic structure after calcination according to X-ray diffraction (XRD). Inhomogeneous strain, calculated using the Williamson–Hall method, was found to increase with palladium content, and the lattice contracts slightly, relative to nano-cerium oxide, as palladium content is increased. Moreover, high resolution transmission electron microscopy reveals some instances of defective microstructure. These factors combined imply that palladium is in solid solution with CeO_2 in these nanoparticles, but palladium (II) oxide (PdO) peaks in the Raman spectra indicate that solid solution formation is partial and that highly dispersed PdO is present as well as the solid solution. Nevertheless, the addition of palladium to the CeO_2 lattice inhibits the growth of the 6% Pd–CeO_2 particles compared to pure CeO_2 between 600 and 850 °C. Activation energies for grain growth of 54 ± 7 and 79 ± 8 kJ/mol were determined for 6% Pd–CeO_2 and pure CeO_2, respectively, along with pre-exponential Arrhenius factors of 10 for the doped sample and 600 for pure cerium oxide.

Abbreviations

XRD	X-ray diffraction
TWC	Three-way catalyst
Ceria	Cerium oxide
Zirconia	Zirconium oxide
PGM	Platinum group metals
HMT	Hexamethylenetetramine
ICP–OES	Ion-coupled plasma/optical emission spectrometry
FWHM	Full-width at half-maximum
CCD	Charge coupled device
TEM	Transmission electron microscopy
HRTEM	High resolution transmission electron microscopy
BNL	Brookhaven National Laboratory
XANES	X-ray absorption near edge spectroscopy
I.C.D.D.	International Centre for Diffraction Data
E_a	Activation energy

H. Liang · J. M. Raitano · G. He · A. J. Akey · I. P. Herman
Department of Applied Physics and Applied Mathematics, Columbia University, New York, NY 10027, USA

L. Zhang
Center for Functional Nanomaterials, Brookhaven National Laboratory, Upton, NY 11973, USA

S.-W. Chan (✉)
Department of Applied Physics and Applied Mathematics, Columbia University, New York, NY 10027, USA
e-mail: sc174@columbia.edu

Introduction

Nanocrystalline cerium oxide (CeO_2), also known as ceria, is now receiving remarkably increased attention as a key component of automotive catalysts, because of its unique redox properties and high oxygen storage capacity, which are crucial for controlling the ratio of oxidants and reductants in automotive exhaust [1]. It can stabilize the dispersion of precious metals and the structure of an alumina support, promote the water–gas shift and steam-reforming reactions, and suppress the strong interaction between the precious metals and alumina [2–4]. In recent years, CeO_2-supported noble metals (NM) have been extensively employed in automotive exhausts and other industrial applications [5–7].

One of the most intriguing scientific aspects of ceria-supported catalysts is that their activity and stability depend strongly on preparation conditions, treatment history, and the presence of additives [3]. Traditionally, NM are impregnated on ceria or ceria–zirconia solid solutions with alumina as carrier in automotive catalysts [8]. However, research has indicated that in conventional catalysts, only the surface atoms of NM particles serve as adsorption sites, and even for 4–6 nm metal particles, only 1/4–1/5 of the total NM atoms are utilized for catalytic conversion [9]. In order to increase the dispersion of NM on CeO_2 and improve its effect on the activity of the catalyst, different catalyst synthesis methods have been developed.

Liu et al. [10] used NaOH as precipitation agent to prepare $Pd/Ce_{0.8}Zr_{0.2}O_2$ catalyst and found that Pd^{2+} ions partially entered into the lattice of ceria–zirconia solid solutions. Catalysts synthesized in this manner show a much higher conversion for methanol decomposition than ones prepared with a traditional impregnation method. Hegde's group developed a solution combustion method to prepare highly dispersed NM ionic catalysts [11, 12]. They found the conversions of CO, NO*x* and hydrocarbons are much higher when NMs were doped into the ceria or titania lattice at the same NM loading concentration. Weng's group [13, 14] prepared Pd-doped CeO_2 catalysts with a citric-aided sol–gel method and found the sample treated at 300 °C produces the highest CO oxidation activity and has the lowest oxygen activation energy due to the enlarged Pd–Ce interface. All these research studies indicate that highly dispersed surface NM combined with NM doped in the lattice lead to high catalytic activity.

Our group had already developed a simple room temperature method to prepare nanoparticulate ceria [15]. In this study, Pd-doped CeO_2 nanocrystalline catalysts were easily obtained based on this method. The structural, chemical, and morphological properties of the co-precipitated nanoparticles are characterized with X-ray diffraction (XRD), transmission electron microscopy (TEM), high resolution transmission electron microscopy (HRTEM), and Raman spectroscopy. Since the deactivation of $Pd–CeO_2$ at high temperature is obviously due to nanoparticle growth [16], the coarsening of co-precipitated $Pd–CeO_2$ nanoparticles is investigated as well.

Experimental

Nanoparticles of palladium-modified cerium oxide ($Pd–CeO_2$) were aqueously co-precipitated as follows. Two solutions were prepared: a 0.0375 M cerium nitrate hexahydrate, $Ce(NO_3)_3{\cdot}6H_2O$ (99.5%, Alfa Aesar), solution to which varying amounts of palladium nitrate, $Pd(NO_3)_2{\cdot}xH_2O$ (99.9%, Alfa Aesar), were added and a 0.5 M hexamethylenetetramine (HMT), $(CH_2)_6N_4$ (>99%, Alfa Aesar) solution (the amount of palladium nitrate used was dependent upon the desired final content and will be specified below). After mixing the solutions separately for 30 min, the two were combined at room temperature and mixed together for 15 min. Then the mixture was heated up to 85 °C in a water-jacketed beaker for 3 h. To help identify the palladium species precipitating from solution, the same procedure was followed in a separate reaction, but no cerium nitrate was used.

Elemental analysis of Pd and Ce was performed by Columbia Analytical Services (Tucson, Arizona) using ion-coupled plasma-optical emission spectrometry, ICP–OES (Perkin Elmer Optima 3000 DV or Thermo Jarrell Ash ICAP 61).

The uncalcined samples and the samples for the activation energy study were examined with an Inel XRG-3000 instrument, which has a curved position-sensitive (CPS) detector with an angular range (2θ) of 1°–110°. The remaining scans, including the lattice parameter study, were obtained using a Philips X'Pert PW3040-Multi-Purpose Diffractometer instrument with an angular (2θ) increment of 0.02° between 23° and 100° and a hold time of 0.5 s. Both instruments employed CuK_{a1} radiation and were operated at 40 kV and 30 mA.

The XRD data were converted from .txt to .cpi using Mark Bowden's ConvX software and fit using XFit [17] software. The lattice parameter values were determined by using the extrapolation function $\cos^2\theta_B/\sin\theta_B$, where θ_B is the Bragg angle [18]. Particle size calculations were made based on XRD broadening of the (111) peak of ceria using the Scherrer equation. The (111) peak was chosen because this is the lowest index peak, and peak broadening due to strain and particle size are most easily separated at low angles [19]. A correction was made to the experimental full-width at half-maximum (FWHM) for instrumental broadening by using the FWHM of the NIST standard reference material (SRM) number 1976, which is a plate of Al_2O_3. Unless indicated otherwise, all crystallite sizes reported in this article are calculated from XRD data.

Raman scattering was performed in a backscattering configuration using the 514.5 nm line of Ar-ion laser (CVI Melles Griot, 35 MAP 431-208) at room temperature. The beam was focused to a spot size of ~3 μm and all incident power was less than 3.8 mw to minimize heating in the samples. A 300-mm focal length spectrometer (Acton SP2356, PI Acton, Trenton, NJ) with three gratings (1800, 600, and 300 grooves/mm) was used to disperse the Raman signal, and a LN digital charge-coupled-device (CCD) detector (spec-10: 400B. PI Acton) was used to detect the spectra. In the 320–1510 cm^{-1} frequency range (resolution ~1 cm^{-1}), plasma lines were used to calibrate the spectrum.

TEM was performed using a JEOL JEM 100CX operating at 100 kV. HRTEM images of lattice and morphology were acquired on JEOL JEM2100f at 200 kV, located at Center for Functional Nanomaterials, Brookhaven National Laboratory (BNL).

Results

After centrifugation of the co-precipitated product, the supernatant is clear and colorless, and the colors of the resulting powders vary from gray to black as the palladium content increases, unlike the yellow color of pure cerium oxide [20]. Elemental analysis by ICP–OES (Table 1) reveals that for the two greatest palladium concentrations, a slightly higher ratio of $mol_{Pd}/(mol_{Pd} + mol_{Ce})$ was found in the final product than was weighed out in the reactants, but for the other palladium contents, the two values were roughly the same. The uncalcined nanoparticles are monodisperse based on TEM results as seen in Fig. 1.

The yield of cerium oxide was calculated for the 0.4% Pd–CeO_2 particles and is a percentage relating the moles of Ce in the product to the moles in the reactant; the palladium content is treated as negligible. The yield increases as the reaction time increases, but the crystallite size changes negligibly (Fig. 2). For example, the nanoparticle diameter is 10 nm after 1.5 h reacting and 11 nm after 3 h reacting.

XRD data of uncalcined 13% Pd–CeO_2 (Fig. 3) are consistent with the International Centre for Diffraction Data (I.C.D.D.) database [21] file for cerium oxide (00-034-0394) except for a small peak around 38.2°, marked with an asterisk. Compared to the I.C.D.D. data files for palladium compounds also shown in Fig. 3, the peak's position is most consistent with the (111) peak of palladium metal (01-087-0637).

To definitively identify the unknown component in the Pd–CeO_2 samples *before calcination*, the synthesis

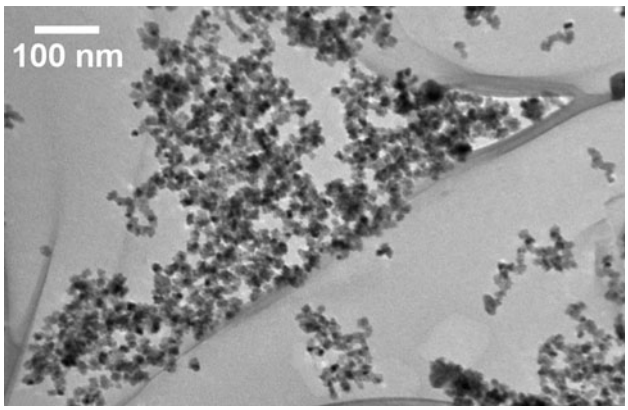

Fig. 1 TEM image of monodisperse 1% Pd–CeO_2 nanoparticles before calcination

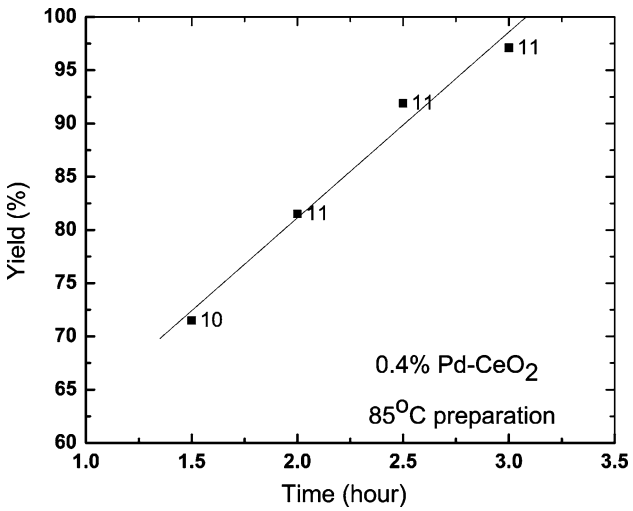

Fig. 2 Particle yield as a function of reaction time for 0.4% Pd–CeO_2 nanoparticles. The diameter of the nanoparticles (in nm) is labeled next to the corresponding points

Table 1 Summary of Pd–CeO_2 nanoparticles synthesized at 85 °C (3 h mixing): $Pd(NO_3)_2$ concentration expressed as molarity (M), precursor and final (ICP) Pd content expressed as an atomic percentage, particle size, and lattice parameter (a_0) of the calcined powders

$[Pd(NO_3)_2]$[a] M	Precursor $\%\frac{mol_{Pd}}{mol_{Pd}+mol_{Ce}}$	ICP–OES $\%\frac{mol_{Pd}}{mol_{Pd}+mol_{Ce}}$[b]	Size (nm)[c]	Lattice parameter (Å)
0.00018	0.5	0.4	11	5.4158 ± 0.0004
0.00039	1	1	10	5.4162 ± 0.0004
0.00073	2	2	9	5.4172 ± 0.0005
0.0015	3.8	6	8	5.418 ± 0.001
0.0029	7.4	13	6	5.420 ± 0.003

[a] $Ce(NO_3)_3$ concentration is constant at 0.0375 M

[b] Relative error in $\%\frac{mol_{Pd}}{mol_{Pd}+mol_{Ce}}$ is ±10%

[c] Size calculated by applying the Scherrer equation to the (111) XRD peak of CeO_2

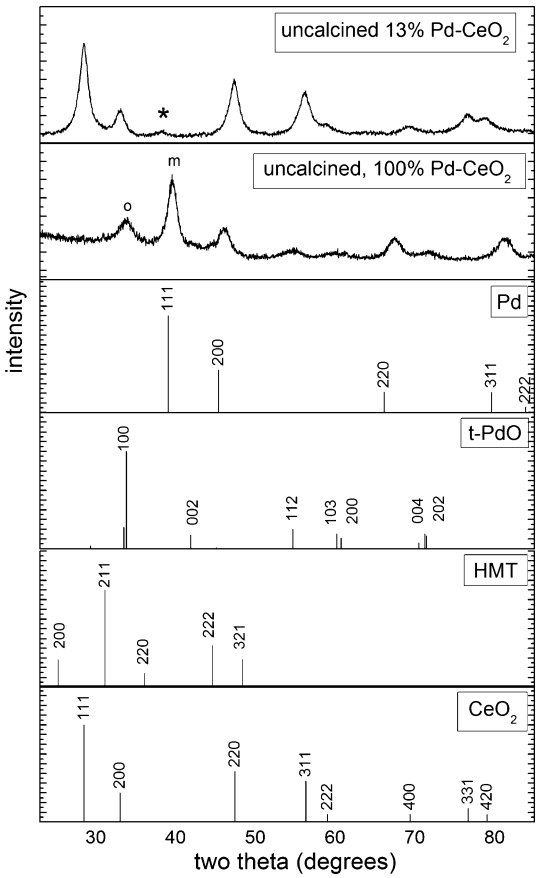

Fig. 3 Uncalcined nanoparticles of 13% Pd–CeO_2 and 100% Pd–CeO_2 and standard powder diffraction data of Pd (01-087-0637), PdO (00-041-1107), hexamethylenetetramine or HMT (00-32-1708), and CeO_2 (00-034-0394). The standards are from the International Centre for Diffraction Data (I.C.D.D.), and the values in parentheses are I.C.D.D. database codes

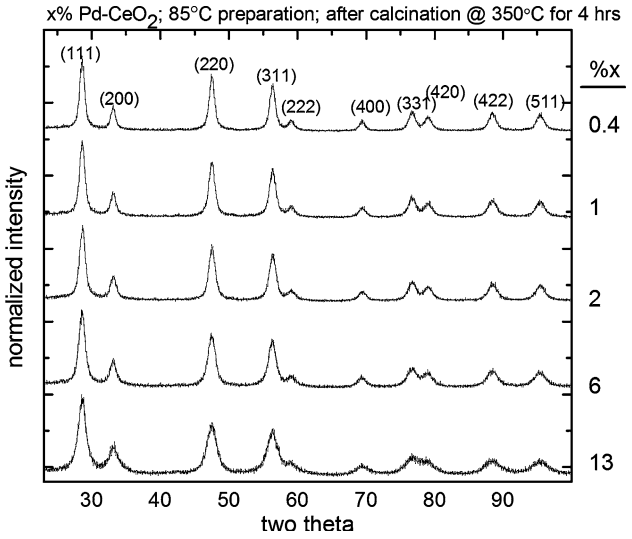

Fig. 4 XRD of calcined *x*Pd–CeO_2 nanoparticles precipitated from solution at 85 °C where *x* is the atomic % Pd in the final product and varies from 0.4 to 13%. Only peaks characteristic of cerium oxide are seen and are indexed. Particle size is indicated to the right of each diffractogram

procedure was essentially repeated without the use of cerium nitrate. The XRD of the uncalcined sample is labeled 100% Pd–CeO_2 (Fig. 3) to emphasize that it was prepared in the same manner as the other samples but with only the palladium salt reactant. This diffractogram was compared to the I.C.D.D. files shown in Fig. 3, as well as commercially purchased $Pd(OH)_2$ and the I.C.D.D. files for $Pd(NO_3)_2$ (00-058-0170), PdO_2 (00-034-1101), $Pd_{0.5}(Pd_3O_4)$ (01-071-1866), and rocksalt-like PdO (46-1211). All of the peaks, except for one at 33.8° (labeled "o"), match the palladium I.C.D.D. metal file mentioned above. In particular, the peak at 38.2° (labeled "m"), which is the most intense of the metallic peaks, is consistent with the previously unknown "*" peak in the uncalcined 13% Pd–CeO_2. The exception peak at 33.8° in 100% Pd–CeO_2 is most consistent with the tetragonal oxide of palladium (t-PdO, 00-041-1107) and was likely present in the diffractogram of the uncalcined 13% Pd–CeO_2 as well, but was obscured by the (200) peak of ceria at 33.0°. Therefore, it is concluded that the 100% Pd–CeO_2 sample is composed of Pd metal and t-PdO, and the samples prepared with cerium nitrate consist of CeO_2, Pd metal, and t-PdO before calcination.

After calcination at 350 °C, the color of the Pd–CeO_2 powder changes to shades of brown, again varying in intensity with palladium content, rather than the yellow color of pure cerium oxide [20] or the gray-to-black color of the precursor. The XRD data show only peaks characteristic of cerium oxide, and these are indexed accordingly (Fig. 4). The lattice parameter shows a slight increase with increasing palladium content, and crystallite (particle) size calculated by the Scherrer equation, decreases with Pd content (Table 1). Moreover, a Williamson–Hall plot for each of the calcined particles reveals that the inhomogeneous strain increases as the Pd content increases (Fig. 5).

Generally, the same Raman peaks are seen throughout the Pd–CeO_2 series (Fig. 6), including the asymmetric, prominent 465 cm^{-1} peak (labeled I_4) and the broad peak around 600 cm^{-1} (labeled I_5). If we examine the former peak more closely (Fig. 6b), it is evident that in the 13% Pd–CeO_2 sample, this peak is shifted to a lower frequency and is much broader than that associated with lower palladium contents. We observe peaks at 640 cm^{-1} (labeled I_{PdO}) and 1122 cm^{-1} (Fig. 6a) as well.

Examination of HRTEM images for two compositions, 1% Pd–CeO_2 and 13% Pd–CeO_2, calcined at 350 °C, shows crystallite sizes to be approximately consistent with calculations based on XRD peak broadening using the Scherrer equation. Specifically, for 1% Pd–CeO_2, the TEM-based size is 8 nm (119 particles' average, images

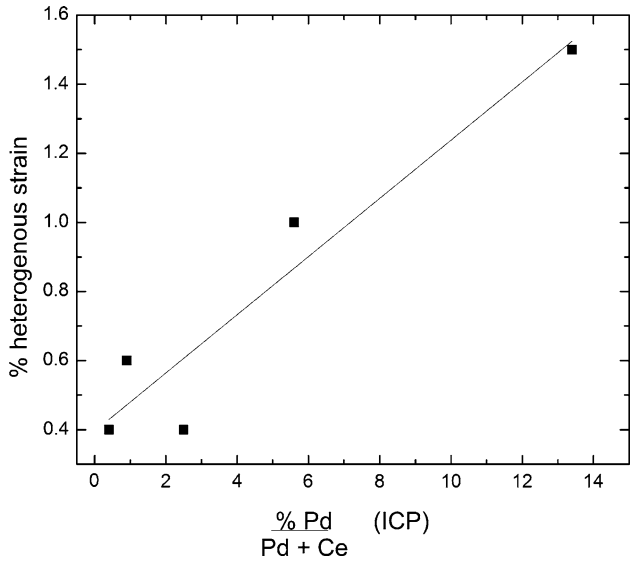

Fig. 5 Inhomogeneous strain in the lattice of Pd–CeO_2 nanoparticles: inhomogeneous strain (%) is directly related to the palladium content of the nanoparticles

not shown), while the XRD-based size is 10 nm (Table 1). For the 13% Pd–CeO_2 sample, the TEM-based size is 9 nm (39 particles' average, representative crystallites shown in Fig. 7) and the XRD-based size is 6 nm (Table 1). Moreover, the morphology of the post-calcination nanoparticles is roughly equiaxed (Fig. 7a, b), and for the highest palladium content studied, 13%, some particles show regions of extended defects (Fig. 7b).

To understand how the presence of palladium in these nanoparticles affects crystallite growth when the particles are subject to heat, pure CeO_2 was studied in comparison to 6% Pd–CeO_2. The palladium content of the latter sample was chosen, because it is approximately in the middle of the composition range studied.

When heated at or above 600 °C, pure CeO_2 and 6% Pd–CeO_2 nanoparticles coarsen. However, the pure CeO_2 crystallites grow more in size over the 600–850 °C temperature interval studied (Fig. 8). For example, at 850 °C, pure CeO_2 has grown in diameter by about 30 nm with respect to the 600 °C size, while 6% Pd–CeO_2 has increased in diameter by about 20 nm.

The activation energy for such coarsening can be calculated by performing several calcinations with different maximum hold temperatures, T, and with different resulting final particle sizes, D, and using the following equation:

$$\frac{D^n - D_0^n}{t} = Ae^{-E_a/RT}, \quad (1)$$

where D_0 = initial grain size, D = final grain size, n = constant related to growth mechanism, t = calcination time, A = pre-exponential factor, E_a = activation energy, R = gas constant or its natural logarithm

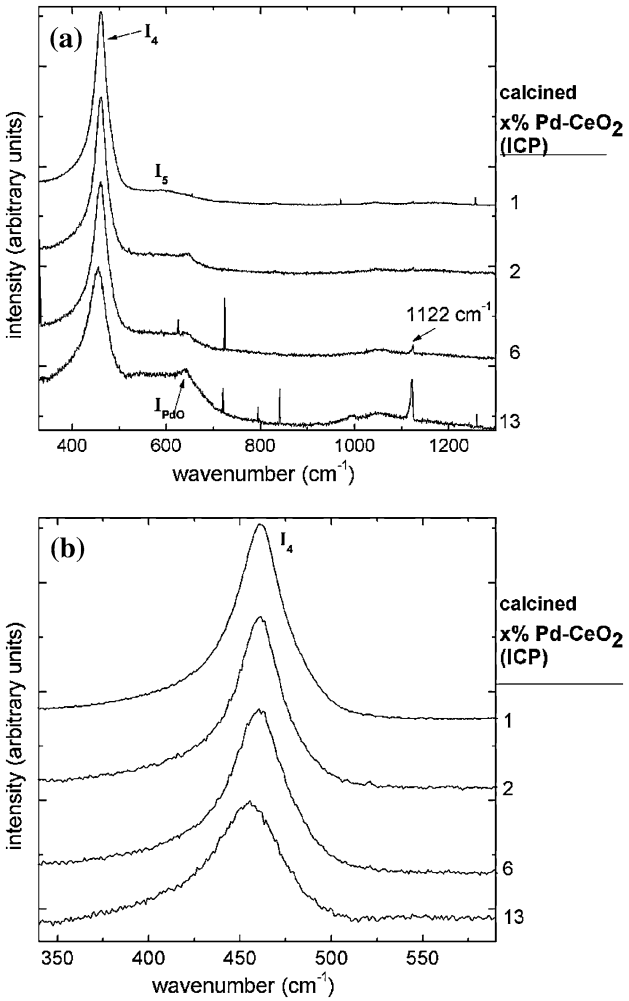

Fig. 6 Raman spectra of Pd–CeO_2 nanoparticles with varying palladium contents **a** complete spectra **b** closeup of primary peak

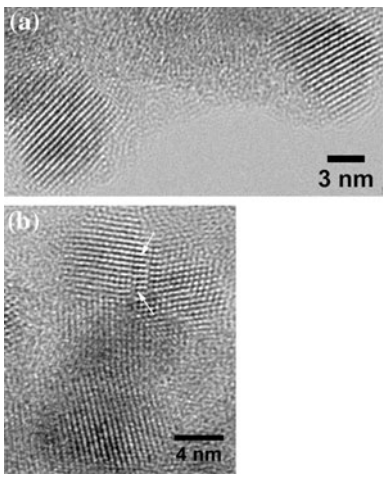

Fig. 7 HRTEM images of calcined 13% Pd–CeO_2 nanoparticles **a** two typical particles **b** another group of particles one of which shows an extended defect marked by *two arrows*. Both sets of nanoparticles were precipitated from solution at 85 °C

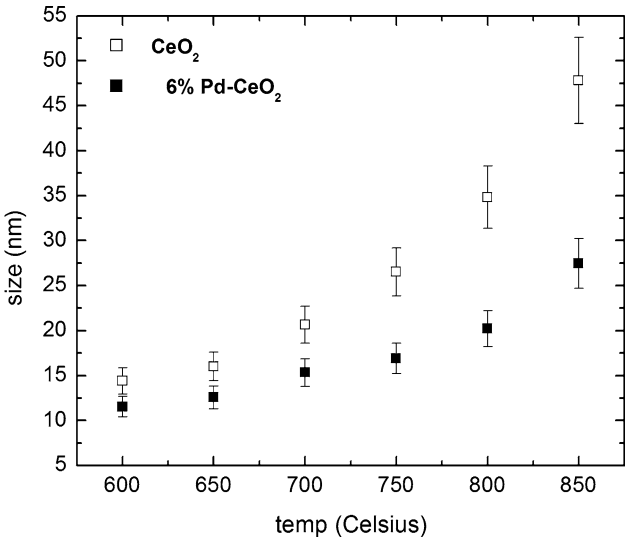

Fig. 8 Nanoparticle size (nm) as a function of calcination temperature for pure CeO_2 and 6% Pd–CeO_2

$$\ln\left[\frac{D^n - D_0^n}{t}\right] = \ln A - \frac{E_a}{RT}. \quad (2)$$

However, when the error in $\ln\left[\frac{D^n - D_0^n}{t}\right]$ is considered, it is clear that plotting this term as a function of reciprocal temperature is problematic. That is, if we assume that the error in particle size with the Scherrer method is roughly ±10% as has been suggested [19] and propagate error through the subtraction of D_0 from D followed by dividing by t and then taking the natural log of the result [22], the y-error bars for the lowest temperatures are significant. Higher temperatures would have somewhat smaller errors, because $D - D_0$ would be larger, but the high relative error for many of the data points would make calculation of a meaningful value of the activation energy impossible. For this reason, the D_0 term is ignored as has been done elsewhere [23].

The exponent, n, which is related to the growth mechanism [24], is taken as 2 for CeO_2 as has been suggested to be appropriate for ceramics in general [25] and ceria in particular [26]. Selecting the exponent for 6% Pd–CeO_2, is more complicated, because extremely undersized dopants, like palladium in ceria have high grain boundary mobility, which implies an exponent of 4 is appropriate in Eq. 1 [24], while solute drag at high dopant concentrations suppresses such mobility [26]. Since others in the literature have used 2 for cerium oxide combined with dopants of similar size, valence, and concentration [27], an exponent of 2 was chosen. A linear fit from 600 to 850 °C performed with Origin software [28] yields an activation energy 79 ± 8 kJ/mol for pure CeO_2 with a pre-exponential factor, A, of 600 and 54 ± 7 kJ/mol for 6% Pd–CeO_2 with an A of 10.

These values were then used to calculate the rate constant for grain growth, k, with the well-known Arrhenius equation, $k = A\ \exp(-E_a/RT)$, in which the terms to the right of the equal sign have been defined in Eq. 1 above. The rate constant is then plotted as a function of temperature for pure and doped CeO_2 (Fig. 10) and was found to be higher for pure CeO_2 than 6% Pd–CeO_2 between 600 and 850 °C.

Discussion

Nanoparticle characterization with an emphasis on structure

For the preparation of the Pd–CeO_2 nanoparticles, the reaction mixing time of 3 h was chosen, because the yield was roughly 100% (Fig. 2), while the particle size changed very little compared to samples collected after shorter mixing times. Note that the size is described as being "unchanged" because the error in particle size using the Scherrer equation is about 10% typically [19]. Therefore, a 1 nm difference between particles that are roughly 10 nm in size is negligible.

The product collected, as indicated above, had a slightly higher value of $\%mol_{Pd}/(mol_{Pd} + mol_{Ce})$ than was weighed out in the reactants at the highest Pd concentrations (i.e., 6 and 13% Pd by ICP–OES). This trend may be attributable to a lower nucleation rate of ceria when the concentration of Pd^{2+} is high as has been observed with the nucleation of calcite in the presence of magnesium ions [29]. This explanation is consistent with the supernatant being clear and colorless after centrifugation, although the precursor, palladium nitrate, is brown. That is, most of the palladium nitrate has reacted, while cerium nitrate, which is colorless [20], could still be present in solution (i.e., unreacted).

According to XRD data, this uncalcined product is a mixture of CeO_2, Pd metal, and t-PdO. The presence of the first two compounds is evident in the XRD of the uncalcined sample (Fig. 3). However, the presence of t-PdO is implied by the product obtained when the reaction is executed without cerium nitrate. Namely, the XRD peak positions of this uncalcined, cerium-free powder are in agreement with those of Pd metal and t-PdO (Fig. 3). Only the Pd metal peak at 38.2° is evident in the XRD of uncalcined 13% Pd–CeO_2, because this peak is the most intense peak of Pd metal. The intensities of the other Pd metal and t-PdO peaks are too weak to be visible above the cerium oxide peaks and the background in 13% Pd–CeO_2.

During calcination, some palladium enters the lattice of nanoparticulate CeO_2 and forms a solid solution. This assertion is partly based on six factors. First, the palladium

peak disappears upon calcination, leaving only fluorite peaks in the XRD (Fig. 4). Second, the color of the nanoparticles changes upon calcination from gray/black to brown. Third, the round shape (Fig. 7) is different than pure ceria, which tends to be octahedrons or truncated octahedrons [30]. Fourth, the lattice parameter of 13% Pd–CeO_2 nanoparticles, provided in Table 1, in particular, is smaller than would be expected for 6 nm particles according to studies on pure nano-ceria, which tends to have an expanded lattice relative to bulk ceria due to a negative Madelung pressure [31] and a non-negligible Ce^{3+} content [32]. In similarly prepared nano-ceria of the same size, the lattice parameter is 5.4330 Å [30], instead of the observed value of 5.420 Å for the 13% Pd–CeO_2 sample. Such a lattice contraction could be due to solid solution formation, since Pd^{2+} is a smaller cation than Ce^{4+} (cation radii of 0.86 and 0.97 Å, respectively) [33]. Fifth, such inhomogeneous strain (Fig. 5) is expected in a system involving cations with dissimilar radii [33] and is further evidence of solid solution formation. Sixth, although nano-ceria prepared in a similar manner exhibits near perfect crystallinity [15], the microstructure in 13% Pd–CeO_2 is somewhat defective (Fig. 7) as might be the case in a solid solution between size-mismatched cations.

Raman spectroscopy shows the triply degenerate F_{2g} peak, the only peak found in perfect crystals of cerium oxide [34], while the broad I_5 peak has been associated with oxygen vacancies in ceria [35] (the peaks are given the labels I_4 and I_5 to be consistent with our earlier study involving cerium oxide [36]). These Raman features further support solid solution formation. Oxygen vacancies would be generated if Pd^{2+} took the place of Ce^{4+} in ceria's fluorite lattice, so the more intense I_5 peak for 13% Pd–CeO_2 compared to 1% Pd–CeO_2 indicates the formation of solid solution (Fig. 6a). Moreover, the greater width of the F_{2g} Raman peak for the 13% Pd–CeO_2 sample compared to 1% Pd–CeO_2 sample (Fig. 6b) may be a byproduct of solid solution formation, because such peak width increases are associated with lattice disorder [37] and inhomogeneous strain [38] as well as decreases in particle size [38]. Since TEM data for the 13% Pd–CeO_2 sample (Fig. 7) show the particle size for this composition is 9 nm, which is comparable to the other compositions, while the Scherrer size is 6 nm, the differences between these sizes is attributable to the high level of inhomogeneous strain in the 13% Pd–CeO_2 sample, as seen in Fig. 5, and further support the formation of a solid solution.

The remaining Raman peaks can be attributed to PdO for which the allowed Raman modes are 651 and 445 cm^{-1} [39] and so indicate that some of the palladium exists as dispersed PdO entities, rather than being entirely in solid solution. The former peak can be clearly seen (Fig. 6a), while the latter is likely obscured by ceria's F_{2g} peak. Similarly, the weak peak around 1120 cm^{-1} (Fig. 6a) has been observed elsewhere in palladium oxide [39] and might be attributable to resonance effects which allow for the appearance of normally forbidden lines [40]; such a resonance effect has been observed in PdO subject to 514.5 nm laser irradiation, the wavelength used in this study [41].

Low levels of segregated PdO might not be visible above the XRD noise level due to peak broadening. For example, in Cu–CeO_2, copper contents less than 15% in ceria are routinely not observed in XRD scans [42]; this is a similar system to Pd–CeO_2 in that Cu^{2+}, like Pd^{2+}, is smaller than Ce^{4+} [33]. Other studies of Cu–CeO_2 state that Cu^{2+} and Ce^{4+} radii are too different in size to allow the oxides to be mutually soluble [43] or that copper forms a monolayer on ceria as copper content is increased based on electromotive force (EMF) measurements [44].

Moreover, partial dopant segregation would lower the effective dopant concentration in the bulk of the grains [45] and would be reflected in the Pd–CeO_2 lattice parameter values; therefore, an empirical formula provided by Kim [46] that predicts fluorite lattice parameter as a function of dopant radius, valence, and concentration should be considered. Using this equation, the radius of palladium in eightfold coordination was sought, because that is the coordination number of Ce^{4+} in the ceria lattice [47]. However, eightfold coordination is not normally observed in palladium [33], so the highest coordination number for which palladium radii data were available, six [48], was used, and a value of 5.32 Å was calculated with the Kim formula for 13% Pd–CeO_2. Despite this difference in the cation coordination numbers for the Ce^{4+} and Pd^{2+} radii used in Kim's equation, the discrepancy between the actual measured lattice parameter for the 13% Pd–CeO_2 sample of 5.42 Å and the formula value of 5.32 Å is large enough to call into question the formation of a complete solid solution between palladium cations and cerium oxide at relatively high palladium contents and strongly suggests that, while there is substantial evidence of solid solution formation, some palladium oxide segregation does occur.

Activation energy for particle coarsening

From the viewpoint of catalysis, the most significant result presented in this article is that the 6% Pd–CeO_2, which is a viable catalyst, shows improved thermal stability compared to the support alone, CeO_2, when subject to the same heat treatments. This resistance to coarsening exhibited by the Pd–CeO_2 catalysts is seen in Fig. 8.

The activation energy of 79 ± 8 kJ/mol calculated for pure CeO_2 (Fig. 9) is smaller than some values in the literature for pure ceria, including 581 kJ/mol for Chen et al. [26], and 731 kJ/mol for Zhang et al. [49], but larger than

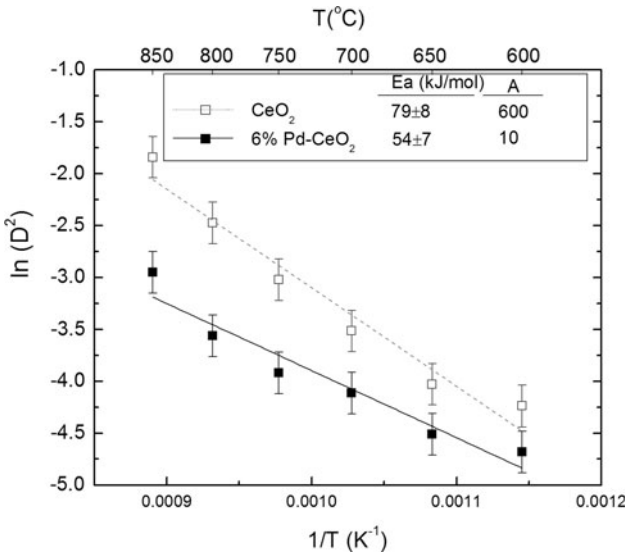

Fig. 9 Calculation of activation energy for coarsening (i.e., growth) in pure CeO_2 and 6% Pd–CeO_2: $\ln(D^2)$ as a function of $1/T$, where D is crystallite diameter, T is the absolute temperature, and n is an exponent related to growth which is taken as 2 for CeO_2 and 6% Pd–CeO_2

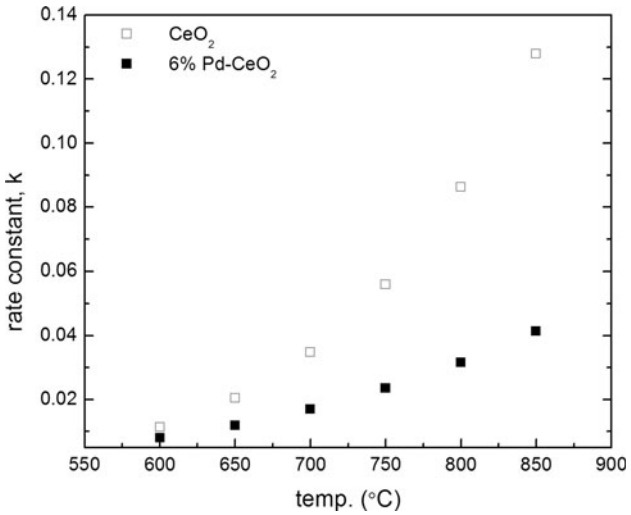

Fig. 10 The rate constant, k, for grain growth as a function of temperature for pure CeO_2 and 6% Pd–CeO_2

the value of 14.6 kJ/mol reported by Hassanzadeh-Tabrizi et al. [23]. The larger values correspond to studies different than this one in that they involved temperatures at or above 1270 °C and were completed with samples that were highly densified, which lessens the influence of porosity on grain boundary mobility [26]. The lower E_a value was calculated differently than ours, using an exponent of 1 in Eq. 1, but also used loose powders and is much closer in magnitude to the value reported here.

However, like many other studies [26, 49–51] of ceria combined with dopants of similar size and valence, the activation energy calculated for 6% Pd–CeO_2 is lower at 54 ± 7 kJ/mol (Fig. 9) than that determined for pure CeO_2. This finding is perhaps surprising, since a depressed activation energy means less energy is needed for crystallites to grow at a given temperature, but Fig. 8 shows that the addition of palladium to ceria inhibited growth.

Yet when these activation energy values are combined in the Arrhenius equation with the pre-exponential constants calculated, 600 for pure CeO_2 and 10 for 6% Pd–CeO_2 (Fig. 9), the rate constant, k, for particle growth is lower for the doped ceria. This is consistent with our finding of depressed growth in the doped sample (Fig. 10). Furthermore, the activation energy and the rate constant of pure ceria are higher than those of 6% Pd–CeO_2 regardless of whether or not the initial particle size D_0 is included in the calculation.

Ultimately, the presence of palladium in the lattice does slow the nanoparticles' growth by disrupting the crystallization of the cerium lattice and probably does so partially by solute drag, which has been noted in ceria samples with as little as 1% of dopants like Mg^{2+} and Ca^{2+} [26].

Conclusions

Nanoparticles of Pd–CeO_2 have been prepared with sizes of 11 nm or less by a simple co-precipitation method. The absence of palladium species in XRD data and an increase in inhomogeneous strain as palladium content increases indicate that some palladium has been successfully doped in the CeO_2 lattice. While Raman spectroscopy supports solid solution formation in the Pd–CeO_2 nanoparticles to some extent, the identification of Raman peaks ascribed to palladium oxide suggests that some palladium exists as PdO, likely in a highly dispersed state. Based on the literature, such a combined structure should have a good catalytic performance. Activity testing of these samples is ongoing and will be published in a following article, but the fact that the 6% Pd–CeO_2 sample does not grow as much as pure CeO_2 between 600 and 850 °C, as has been shown here, is by itself an useful property for a potential catalyst and suggests that this combined structure is effective.

Acknowledgements The authors gratefully acknowledge the support of BASF, the Department of Energy under Award Number DOE DE-FG02-05ER15730, and the Materials Research Science and Engineering Center (MRSEC) Program of the National Science Foundation (# DMR-0213574). Research carried out in part at the Center for Functional Nanomaterials, Brookhaven National Laboratory was supported by the US Department of Energy, Office of Basic Energy Sciences, under Contract No. DE-AC02-98CH10886. Use of the National Synchrotron Light Source, Brookhaven National Laboratory, was supported by the US Department of Energy, Office of Science, Office of Basic Energy Sciences, under Contract No. DE-AC02-98CH10886.

References

1. Han WQ, Wen W, Hanson JC, Teng XW, Marinkovic N, Rodriguez JA (2009) J Phys Chem C 113(52):21949. doi:10.1021/jp9066444
2. Wang XH, Lu GZ, Guo Y, Jiang LZ, Guo YL, Li CZ (2009) J Mater Sci 44(5):1294. doi:10.1007/s10853-009-3275-4
3. Gorte RJ (2010) AIChE J 56(5):1126. doi:10.1002/aic.12234
4. Gorte RJ, Zhao S (2005) Catal Today 104(1):18. doi:10.1016/j.cattod.2005.03.034
5. Costa LOO, Vasconcelos SMR, Pinto AL, Silva AM, Mattos LV, Noronha FB, Borges LEP (2008) J Mater Sci 43(2):440. doi:10.1007/s10853-007-1982-2
6. Colussi S, Trovarelli A, Vesselli E, Baraldi A, Comelli G, Groppi G, Llorca J (2010) Appl Catal A Gen 390(1–2):1. doi:10.1016/j.apcata.2010.09.033
7. Bera P, Hegde MS (2010) J Indian Inst Sci 90(2):299
8. Jen HW, Graham GW, Chun W, McCabe RW, Cuif JP, Deutsch SE, Touret O (1999) Catal Today 50(2):309. doi:10.1016/S0920-5861(98)00512-4
9. Hegde MS, Madras G, Patil KC (2009) Acc Chem Res 42(6):704. doi:10.1021/ar800209s
10. Liu YY, Hayakawa T, Ishii T, Kumagai M, Yasuda H, Suzuki K, Hamakawa S, Murata K (2001) Appl Catal A Gen 210(1–2):301. doi:10.1016/S0926-860X(00)00817-6
11. Dutta G, Waghmare UV, Baidya T, Hegde MS, Priolkar KR, Sarode PR (2006) Chem Mater 18(14):3249. doi:10.1021/cm060267i
12. Roy S, Marimuthu A, Hegde MS, Madras G (2007) Appl Catal B Environ 71(1-2):23. doi:10.1016/j.apcatb.2006.08.005
13. Wang B, Weng DA, Wu XD, Fan J (2010) Catal Today 153(3–4):111. doi:10.1016/j.cattod.2010.02.013
14. Wang B, Weng DA, Wu XD, Ran R (2011) Appl Surf Sci 257(9):3878. doi:10.1016/j.apsusc.2010.11.083
15. Zhang F, Jin Q, Chan S-W (2004) J Appl Phys 95(8):4319. doi:10.1063/1.1667251
16. Shen WJ, Kobayashi A, Ichihashi Y, Matsumura Y, Haruta M (2001) Catal Lett 73(2–4):161. doi:10.1023/A:1016670505059
17. Cheary RW, Coelho AA (1997) Program XFit. In: CCP14 Powder Diffraction Library, Engineering and Physical Sciences Research Council, Daresbury Laboratory, Warrington. http://www.ccp14.ac.uk/tutorial/xfit-95/xfit.htm. Accessed 29 July 2009
18. Cullity BD, Stock SR (2001) Elements of X-ray diffraction. Prentice-Hall, Upper Saddle River
19. Suryanarayana C, Norton MG (1998) X-ray diffraction: a practical approach. Plenum Press, New York
20. Lide DR (ed) (2009–2010) CRC handbook of chemistry and physics, 90th edn. CRC Press, Cleveland
21. International centre for diffraction data (2007) PDF-4. International Centre for Diffraction Data, Newton Square
22. Taylor JR (1982) An introduction to error analysis: the study of uncertainties in physical measurements. University Science Books, Mill Valley
23. Hassanzadeh-Tabrizi SA, Mazaheri M, Aminzare M, Sadrnezhaad SK (2010) J Alloy Compd 491:499. doi:10.1016/j.jallcom.2009.10.243
24. Coster M, Arnould X, Chermant JL, Chermant L, Chartier T (2005) J Eur Ceram Soc 25:3427. doi:10.1016/j.jeurceramsoc.2004.09.003
25. El-Khozondar R, El-Khozondar H, Gottstein G, Rollet A (2006) Egypt J Solids 29(1):35
26. Chen P-L, Chen I-W (1996) J Am Ceram Soc 79:1793. doi:10.1111/j.1151-2916.1996.tb07997.x
27. Li JG, Ikegami T, Mori T (2004) Acta Mater 52(8):2221. doi:10.1016/j.actamat.2004.01.014
28. Origin. Ver. 8.0988 (1991–2009) Origin Lab Corporation, Northampton, MA
29. Bischoff JL (1968) J Geophys Res 73(10):3315
30. Zhang F, Chan S-W, Spanier JE, Apak E, Jin Q, Robinson RD, Herman IP (2002) Appl Phys Lett 80(1):127. doi:10.1063/1.1430502
31. Perebeinos V, Chan S-W, Zhang F (2002) Solid State Commun 123(6–7):295
32. Zhang F, Wang P, Koberstein J, Khalid S, Chan S-W (2004) Surf Sci 563(1–3):74. doi:10.1016/j.susc.2004.05.138
33. Lide DR (ed) (2011) CRC handbook of chemistry and physics, Electronic edn. CRC Press, Boca Raton
34. Keramidas VG, White WB (1973) J Chem Phys 59(1):1561. doi:10.1063/1.1680227
35. McBride JR, Hass KC, Poindexter BD, Weber WH (1994) J Appl Phys 76(4):2435
36. Zhang F, Chen C-H, Hanson JC, Robinson RD, Herman IP, Chan S-W (2006) J Am Ceram Soc 89(3):1028. doi:10.1111/j.1551-2916.2005.00788.x
37. Davydov VY, Goncharuk IN, Baidakova MV, Smirnov AN, Subashiev AV, Aderhold J, Stemmer J, Rotter T, Uffmann D, Semchinova O (1999) Mater Sci Eng B Solid State Mater Adv Technol 59(1–3):222. doi:10.1016/S0921-5107(98)00370-5
38. Spanier JE, Robinson RD, Zhang F, Chan S-W, Herman IP (2001) Phys Rev B 64(24):245407. doi:10.1103/PhysRevB.64.245407
39. McBride JR, Hass KC, Weber WH (1991) Phys Rev B 44(10):5016. doi:10.1103/PhysRevB.44.5016
40. Rousseau DL, Bauman RP, Porto SPS (1981) J Raman Spectrosc 10:253
41. Weber WH, Baird RJ, Graham GW (1988) J Raman Spectrosc 19(4):239
42. Qi X, Flytzani-Stephanopoulos M (2004) Ind Eng Chem Res 43(12):3055. doi:10.1021/ie0306170
43. Groza JR, Gibeling JC (1993) Mater Sci Eng A A171(1–2):115. doi:10.1016/0921-5093(93)90398-X
44. Knauth P, Schwitzgebel G, Tschope A, Villain S (1998) J Solid State Chem 140(2):295. doi:10.1006/jssc.1998.7890
45. Tschope A (2005) J Electroceram 14:5. doi:10.1007/s10832-005-6580-6
46. Kim D-J (1989) J Am Ceram Soc 72(8):1415. doi:10.1111/j.1151-2916.1989.tb07663.x
47. Mogensen M, Sammes NM, Tompsett GA (2000) Solid State Ion Diffus React 129(1–4):63. doi:10.1016/S0167-2738(99)00318-5
48. Shannon RD (1976) Acta Crystallogr A32:751. doi:10.1107/S0567739476001551
49. Zhang TS, Ma J, Kong LB, Zeng ZQ, Hing P, Kilner JA (2003) Mater Sci Eng B Solid State Mater Adv Technol 103(2):177. doi:10.1016/s0921-5107(03)00198-3
50. Zhang TS, Hing P, Huang HT, Kilner J (2002) Mater Lett 57(2):507
51. Zhang TS, Hing P, Huang HT, Kilner J (2002) J Eur Ceram Soc 22(1):27